

Article

Significance of Ternary Hybrid Nanoparticles on the Dynamics of Nanofluids over a Stretched Surface Subject to Gravity Modulation

Meznah M. Alanazi ¹, Awatif Ahmed Hendi ¹, N. Ameer Ahammad ², Bagh Ali ^{3,*} , Sonia Majeed ⁴
and Nehad Ali Shah ^{5,*}

- ¹ Department of Physics, College of Science, Princess Nourah bint Abdulrahman University, P.O. Box 84428, Riyadh 11671, Saudi Arabia
² Department of Mathematics, Faculty of Science, University of Tabuk, P.O. Box 741, Tabuk 71491, Saudi Arabia
³ School of Mechanical Engineering and Automation, Harbin Institute of Technology, Shenzhen 518055, China
⁴ Department of Mathematics, University of the Punjab, Lahore 54590, Pakistan
⁵ Department of Mechanical Engineering, Sejong University, Seoul 05006, Republic of Korea
* Correspondence: baghalisewag@mail.nwpu.edu.cn (B.A.); nehadali199@sejong.ac.kr (N.A.S.)

Abstract: Boosting the heat transfer rate in a base fluid is of interest to researchers; many traditional methods have been utilized to do this. One significant way is using nanofluid to boost thermal performance. This investigation sought to improve the transmission of a thermal above-stretching inclined surface over an upper surface to be influenced by the magnetic field B_0 along the microgravity $g^*(\tau) = g_0(1 + a \cos(\pi\omega t))$. The G-jitter impacts were analyzed for three colloidal fluids flow; the mono micropolar nanofluid (alumina/water), micropolar hybrid nanofluid (alumina–titanium)/water, and micropolar trihybrid nanofluid (alumina–titanium–silicon)/water. Using suitable transformation, the governing formulation was changed into an ordinary differential equation. In a Matlab script, a computational code was composed to evaluate the impacts of the involved parameters on fluid dynamics. The fluid flow motion and thermal performance for the trihybrid case were greater than the mono and hybrid nanofluid cases subject to a microgravity environment. The fluid velocity and microrotation function decreased in opposition to the magnetic parameter’s increasing strength, but with an increasing trend in the fluid temperature function. Fluctuations in the velocity gradient and heat flow gradient increased as the modulation amplitude increased.

Keywords: FEM; G-jitter; trihybrid nanoparticles; MHD; stretch surface

MSC: 35Q30; 76D05; 76R10



Citation: Alanazi, M.M.; Ahmed Hendi, A.; Ahammad, N.A.; Ali, B.; Majeed, S.; Shah, N.A. Significance of Ternary Hybrid Nanoparticles on the Dynamics of Nanofluids over a Stretched Surface Subject to Gravity Modulation. *Mathematics* **2023**, *11*, 809. <https://doi.org/10.3390/math11040809>

Academic Editors: Nikolay M. Zubarev and Evgeny A. Kochurin

Received: 6 January 2023
Revised: 24 January 2023
Accepted: 29 January 2023
Published: 5 February 2023



Copyright: © 2023 by the authors. Licensee MDPI, Basel, Switzerland. This article is an open access article distributed under the terms and conditions of the Creative Commons Attribution (CC BY) license (<https://creativecommons.org/licenses/by/4.0/>).

1. Introduction

The colloidal combination of a base fluid with one type of nanoparticle is called a nanofluid. This type of fluid is exceptionally valuable in thermal management and cooling, fluid temperature enhancement and diminution, pharmaceutical processes, and microelectronics. Profound investigations into this fluid revealed that it contains two types of nanoparticles that are heavily mixed with the base fluid (i.e., a hybrid nanofluid). At different temperatures, the alumina-based fluid dynamic viscosity changes with nanoparticle shapes [1]. The different shapes of tiny particles have differences in the interactions and agglomeration, and host fluids are associated with surface charges. Recently, the colloidal combination of three different types of tiny particles of nanoparticles subject to one base fluid—the trihybrid nanofluid—has started; the results of a couple of investigations appear to be insightful and encouraging. The thermal analysis of a mass ratio 4:4:2 to produce carbon nanotubes and carbonate nanofluid shows that it is beneficial with super-critical power plants because of thermal diffusiveness along the stability, which enhance negligibility due to increments in heat transfer (Sang et al. [2]). Mousavi et al. [3] explored the dynamics of the H₂O transmission of magnesium and copper oxide with titanium oxide. Sahoo and

Kumar [4] investigated the thermal characteristics of water-transmitting titanium oxide and copper oxide alumina nanoparticles (ternary hybrid nanofluid). The heat transfer in the base fluid was enhanced due to various shapes of nano-sized particles [5] and trihybrid fluid temperatures were higher compared to the single and two-type nanoparticle suspensions with base fluids [6].

The majority of the time, in microgravity or low gravity environments, the existence of temperature differences and gravitational fields can produce buoyancy convective fluxes. In this situation, sedimentation and the flow of buoyancy-driven fluid highly decreased. This G-jitter impact has been focused on by many researchers (in many geometries and conditions). There are numerous uses for G-jitter convection, including crew motion, sprays, spacecraft, etc. Following Sharidan et al. [7], the gravity acceleration takes the following form: $g^*(t) = g_o[1 + \epsilon \cos(\pi\omega t)]k$. Here, $g^*(t)$, acting for unit vector k , presents an upward direction, ϵ represents the scaling parameter, g_o shows the average time value of the gravitational acceleration, t is the time, and ω shows the frequency of the G-jitter-driven flux oscillation. Many physical aspects of the investigated works have illustrated certain attributes, such as the G-jitter magnetic hydrodynamic flux [8], the Jeffrey fluid with a microgravity-inclined surface [9], the analysis of the heat-transferred rate with the existence of G-jitter [10], non-Newtonian fluids with impacts on the G-jitter force [11,12].

There is interest in non-Newtonian analyses since these fluids are largely encountered in the industry and physiology. Bile, blood, animal and human feces, chyme, lubricants, paints, and oils are common examples of non-Newtonian fluids. One significant obstacle in the analysis of such fluids is the failure of a single constitutive equation from the Newtonian fluid model to accurately predict the behaviors of these fluids. Various models of fluids capable of successfully predicting the fluid's viscoelastic behaviors were offered to fill this gap. Presently, non-Newtonian fluids play vital roles in several industrial implementations, such as polymer, plastic production, the manufacturing of paper, and in various technological processes. Shehzad et al. [13] studied the impacts of multi-layer coatings of MHD non-Newtonian and Newtonian liquids by a porous-inclined rotational channel. Awan et al. [14] studied the significance of aggregation of Coriolis forces based on non-Newtonian. Ali et al. [15] analyzed the significance of mixed convection and hydrodynamics with Casson-based fluid over the stagnation point of a spinning sphere via FEM simulations. Koriko et al. [16] explained the impacts of magnetic flux and melting temperature transportation on non-Newtonian liquid flux toward the stagnation point. Abiev et al. [17] illustrated the two-phase mathematical model—Taylor flux hydrodynamics for four Newtonian and non-Newtonian liquids in microchannels.

Various analysts and researchers have investigated the magnetohydrodynamic (MHD) fluxes of materials across surfaces with tremendous thermophysical attributes, heat transmission performances, and valuable uses in daily life. MHD utilizations may emerge in astrophysics sensors, magnetic drug targeting, and engineering; in particular, in forming the stars, magnetic fields play a vital role. Due to these lasting benefits, researchers and investigators are inspecting MHD flux. MHD applications cover large ranges of physical areas. They are used in industrial equipment, physics, chemistry, and engineering implementations, such as boundary layer control, petroleum, and pumps. In the last few decades, research into significant MHD applications has been conducted [18–21]. There is inherent trouble in seeking solutions in the non-linearity connected with the convective terms of mathematical formulations. Such types of problems have been tackled using different numerical techniques, such as the RK method, BVP4c, boundary element, finite volume, finite difference, spectral element method [22], etc. The FEM is one of the most famous and powerful numerical tools; it has been used by numerous developers and users to numerically solve complex types of engineering problems. Many researchers use this technique to solve boundary value problems subject to various shapes of geometries [23–25].

Recently, augmented thermal operations have enhanced missions as a result of contemporary technological advancements. Utilizing nanoparticles has made it possible to meet expanding demands in large quantities. The primary aim of this study is to show the

influence of trihybrid nanoparticles on the dynamics of a micropolar nanofluid subjected to an inclined–extended surface in the presence of a regularly changing gravity environment. The above studies show that less consideration is given to this study; this report will be useful for experts to explore various features and analyze the different outcomes. In a recent analysis, the FEM simulation was intended to clarify the effects of flow on microgravity on the flow and temperature characteristics of Al₂O₃, TiO₂, SiO₂, and H₂O (trihybrid nanofluids) due to an inclined extending surface. The present inquiry seeks to answer the following research questions:

- What effects do the Lorentz force, micropolar material, and trihybrid nanofluid heat transfer have when there is microgravity?
- What are the differences between trihybrid, hybrid, and mono nanofluids in terms of heat distribution and flow that are affected by microgravity?
- How does one observe the effects of the frequencies of oscillation and modulation amplitudes for trihybrid, hybrid, and mono nanofluids with G-jitter due to inclined and raised surfaces in higher dimensional spaces?

2. Flow Model Mathematical Formulation

Here, we examine the influence of microgravity on the flow of non-Newtonian fluid and the thermal attributes of Al₂O₃, TiO₂, SiO₂, and H₂O (trihybrid nanofluid) because of the extended surface, as presented in Figure 1. In this report, γ , B_o , T_∞ , and T_w are inclined angles, a uniform magnetic field in the y-direction, the ambient value of the temperature, and the constant temperature, respectively. The normal axis of the surface is the y-axis; along the x-axis, the surface is extending. Moreover, it is assumed that the linear velocity is $u_w = bx$ ($b > 0$). Thermophysical characteristics of H₂O (water-based fluid), Al₂O₃, TiO₂, and SiO₂ (ternary nanoparticles) are shown in Table 1, and no slip occurs between the tiny particles and water-based fluid; solid particles are in thermal equilibrium. Solid particle agglomeration is ignored due to the mixture. Further, the momentum equation associated with the gravitational field is affected by $g^*(t) = g_o[1 + \epsilon \cos(\pi\omega t)]k$. The mass, linear momentum, angular momentum, and energy (heat) conservation governing equations for the trihybrid nanofluid can be written as [26,27]:

$$\partial_x \tilde{u}_o + \partial_y \tilde{v}_o = 0, \tag{1}$$

$$\rho_{n_f} (\partial_t \tilde{u}_o + \tilde{u}_o \partial_x \tilde{u}_o + \tilde{v}_o \partial_y \tilde{u}_o) = (\mu_{n_f} + \kappa) \partial_{yy} \tilde{u}_o - \sigma B_o^2 \tilde{u}_o + \kappa \partial_y \tilde{N} + g^*(t) (\rho_{n_f} \beta) (\tilde{T} - \tilde{T}_\infty) \cos \alpha, \tag{2}$$

$$j \rho_{n_f} (\partial_t \tilde{N} + \tilde{u}_o \partial_x \tilde{N} + \tilde{v}_o \partial_y \tilde{N}) = \gamma^* (\mu_{n_f} + \frac{\kappa}{2}) \partial_{yy} \tilde{N} - \kappa (2N + \partial_x \tilde{u}_o) \tag{3}$$

$$\partial_t \tilde{T} + \tilde{u}_o \partial_x \tilde{T} + \tilde{v}_o \partial_y \tilde{T} = \tilde{\alpha} \partial_{yy} \tilde{T}. \tag{4}$$

where the $(\tilde{u}_o, \tilde{v}_o)$ velocity variables along x, y, \tilde{N} & \tilde{T} represent the angular velocities with the temperature of the fluid, $(\rho_{n_f}, \kappa, C_p, \mu_{n_f}, \tilde{\alpha}, \gamma^*, \beta, \sigma)$, and are, respectively, the density, vortex viscosity, specific heat of the fluid, dynamical viscosity, thermo-diffusivity, viscosity spin gradient of fluid, thermal expansion, and electric conduction. Ali et al.'s [28] spin gradient of fluid viscosity is taken into account $\gamma^* = \mu_{n_f} (j + \frac{\kappa}{2} j)$; here, $K = \kappa / \mu_{n_f}$, presents the material parameter, and elaborates on the problem of the necessary boundary conditions [11,12]:

$$\left. \begin{aligned} t = 0 : \tilde{u}_o = \tilde{v}_o = 0, \tilde{T} = \tilde{T}_\infty, \\ t > 0 : \tilde{u}_o = \tilde{u}_w, \tilde{v}_o = 0, \tilde{N} = 0, \tilde{T} = \tilde{T}_w, \text{ as } y = 0, \\ \tilde{u}_o \rightarrow 0, \tilde{N} \rightarrow 0, \tilde{T} \rightarrow \tilde{T}_\infty, \text{ as } y \rightarrow \infty. \end{aligned} \right\} \tag{5}$$

Table 1. Water and thermophysical properties of nanoparticles [29–31].

Physical Properties	Al ₂ O ₃	TiO ₂	SiO ₂	H ₂ O
ρ	3970.0	4250	2270	0991.1
C_p	0765.0	690	765	4179.0
κ	0040.0	8.953	1.4013	00.613

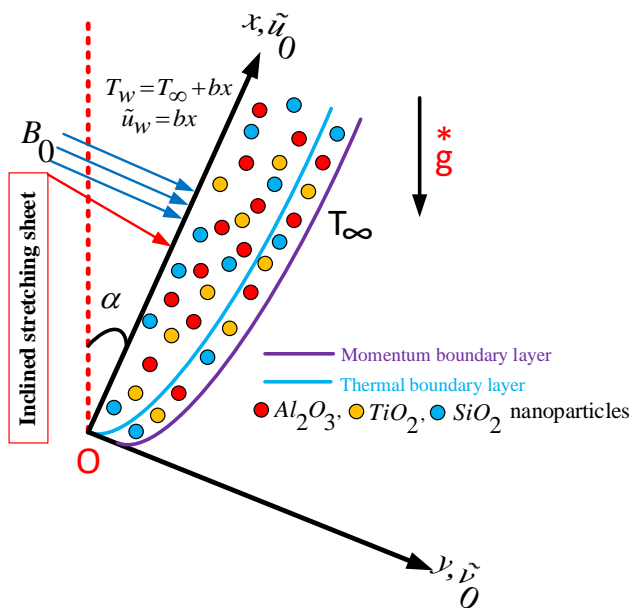


Figure 1. Physical model of developed trihybrid nanofluid model.

The mathematical formula for thermal physical attributes of mono, hybrid, and trihybrid nanofluids [32,33] are as follows:

1. Density

$$\begin{aligned} \mu_{nf} &= \mu_f(1 - \Phi)^{-2.5}, \\ \mu_{hnf} &= \mu_f(1 - \Phi_2)^{-2.5}(1 - \Phi_1)^{-2.5}, \\ \mu_{Thnf} &= \mu_f(1 - \Phi_1)^{-2.5}(1 - \Phi_2)^{-2.5}(1 - \Phi_3)^{-2.5}, \end{aligned}$$

2. Viscosity

$$\begin{aligned} \rho_{nf} &= \Phi\left(\frac{\rho_s}{\rho_f}\right) + (1 - \Phi), \\ \rho_{hnf} &= \Phi_2\rho_{s2} + (1 - \Phi_2)\left((1 - \Phi_1) + \Phi_1\frac{\rho_{s1}}{\rho_f}\right), \\ \rho_{Thnf} &= \left[(1 - \Phi_1)\left[(1 - \Phi_2)\left((1 - \Phi_3)(\rho_f + \rho_3\Phi_3)\right) + (\rho_2\Phi_2)\right] + \rho_1\Phi_1\right], \end{aligned}$$

3. Heat Capacity

$$\begin{aligned} (\rho C_p)_{nf} &= \Phi\left(\frac{(\rho C_p)_s}{(\rho C_p)_f}\right) + (1 - \Phi), \\ (\rho C_p)_{hnf} &= (1 - \Phi_2)\left((1 - \Phi_1) + \Phi_1\frac{(\rho C_p)_{s1}}{(\rho C_p)_f}\right) + \Phi_2(\rho C_p)_{s2}, \\ (\rho C_p)_{Thnf} &= (1 - \Phi_1)\left((1 - \Phi_2)\left[(1 - \Phi_3)(\rho C_p)_f + (\rho C_p)_{s3}\Phi_3\right] + (\rho C_p)_{s2}\Phi_2\right) + (\rho C_p)_{s1}\Phi_1, \end{aligned}$$

4. Thermal Conductivity

$$\begin{aligned} \frac{k_{nf}}{k_f} &= \frac{k_3 + 2k_{nf} - 2\Phi_3(k_{nf} - k_3)}{k_3 + 2k_{nf} + \Phi_3(k_{nf} - k_3)}, \\ \frac{k_{hnf}}{k_{nf}} &= \frac{k_2 + 2k_{nf} - 2\Phi_2(k_{nf} - k_2)}{k_2 + 2k_{nf} + \Phi_2(k_{nf} - k_2)}, \\ \frac{k_{Thnf}}{k_{hnf}} &= \frac{k_1 + 2k_{nf} - 2\Phi_1(k_{nf} - k_1)}{k_1 + 2k_{nf} + \Phi_1(k_{nf} - k_1)}. \end{aligned}$$

In the above formulas, T_{hnf} reflects the ternary hybrid nanofluid, h_{nf} represents the hybrid nanofluid, n_f denotes the nanofluid, and Φ_1 , Φ_2 , and Φ_3 are the volume fractions of the first, second, and third types of nanoparticles, respectively. We use the following non-dimensional variables (see [26]) to reduce the complexity of the elaborated problem.

$$\eta = \sqrt{\frac{\tilde{a}y^2}{\nu}}, \psi = \sqrt{a\nu}xF(\tau, \eta), \tau = a\omega, N = \sqrt{\frac{\tilde{a}}{\nu}}H(\tau, \eta), \theta(\tau, \eta) = \frac{\tilde{T} - \tilde{T}_\infty}{\tilde{T}_w - \tilde{T}_\infty}, \tag{6}$$

where $\psi = \sqrt{a\nu}xF(\tau, \eta)$ is a stream function that obeys the continuity; Equation (1) can be defined as $\tilde{u}_o = \partial\psi/\partial y$ and $\tilde{v}_o = -\partial\psi/\partial x$. By using Equation (6) in the governing equations, the following transformed governing equations are obtained:

$$\left(\frac{1}{\chi_1} + K\right)F''' + \chi_2FF'' - \chi_2F'^2 - MF' + \chi_3\lambda\theta(1 + a \cos \pi\tau) \cos \alpha + KH' = \chi_2\Omega \frac{\partial F'}{\partial \tau}, \tag{7}$$

$$\left(\frac{1}{\chi_1} + 0.5K\right)H'' - \chi_2F'H + \chi_2FH' - K(2H + F'') = \chi_2\Omega \frac{\partial H}{\partial \tau}, \tag{8}$$

$$\chi_4\theta'' + Pr\chi_5F\theta' - Pr\chi_5F'\theta = Pr\chi_5\Omega \frac{\partial \theta}{\partial \tau}, \tag{9}$$

$$\left. \begin{aligned} F(\tau, \eta = 0) = H(\tau, \eta = 0) = 0, F'(\tau, \eta = 0) = 1, \theta(\tau, \eta = 0) = 1, \\ F'(\tau, \eta \rightarrow \infty) \rightarrow 0, H(\tau, \eta \rightarrow \infty) \rightarrow 0, \theta(\tau, \eta \rightarrow \infty) \rightarrow 0, \end{aligned} \right\} \tag{10}$$

where

$$\begin{aligned} \chi_1 &= (1 - \Phi_1)^{-2.5}(1 - \Phi_2)^{-2.5}(1 - \Phi_3)^{-2.5}, \chi_4 = \frac{k_{Thnf}}{k_f}, \\ \chi_2 &= \left[(1 - \Phi_1) \left((1 - \Phi_2) \left[(1 - \Phi_3) + \frac{\rho_3}{\rho_f} \Phi_3 \right] + \frac{\rho_2}{\rho_f} \Phi_2 \right) + \frac{\rho_1}{\rho_f} \Phi_1 \right], \\ \chi_3 &= \left[(1 - \Phi_1) \left((1 - \Phi_2) \left[(1 - \Phi_3) + \frac{(\rho\beta)_{s3}}{(\rho\beta)_f} \Phi_3 \right] + \frac{(\rho\beta)_{s2}}{(\rho\beta)_f} \Phi_2 \right) + \frac{(\rho\beta)_{s1}}{(\rho\beta)_f} \Phi_1 \right], \\ \chi_5 &= \left[(1 - \Phi_1) \left((1 - \Phi_2) \left[(1 - \Phi_3) + \frac{(\rho C_p)_{s3}}{(\rho C_p)_f} \Phi_3 \right] + \frac{(\rho C_p)_{s2}}{(\rho C_p)_f} \Phi_2 \right) + \frac{(\rho C_p)_{s1}}{(\rho C_p)_f} \Phi_1 \right]. \end{aligned} \tag{11}$$

In the above Equations (7)–(9), the dimensionalized frequency is $\Omega = \frac{\omega}{\tilde{b}}$, the magnetic field is $M = \frac{\sigma B_0^2}{b\rho_{nf}}$, the thermal buoyancy is $\lambda = \frac{g_0\beta(\tilde{T}_w - \tilde{T}_\infty)x^3/\nu^2}{(u_w x/\nu)^2}$, Prandtl number is $Pr = \frac{\nu}{\tilde{\alpha}}$, and the material parameter is $K = \frac{\kappa}{\mu_f}$. The Nusselt number and skin friction coefficient expressions are defined as:

$$Nu = \frac{xq_w}{\kappa(\tilde{T}_w - \tilde{T}_\infty)}, C_f = \frac{2\tau_w}{\rho_{nf}u_w^2}, \tag{12}$$

the surface skin friction tensor $\tau_w = ((\mu(T) + \kappa)\partial_y \tilde{u}_1 + \kappa N)_{y=0}$ and thermal flux at surface $q_w = -\kappa(\partial_y \tilde{T})_{y=0}$. In view of Equation (6), we have

$$\left\{ Cf_x Re_x^{1/2} = \left(\frac{1}{\chi_1 \chi_2} + K\right) F''(\tau, 0), Nu_x Re_x^{-1/2} = -\chi_4 \theta(\tau, 0). \right. \tag{13}$$

3. Numerical Procedure

A potent method for dealing with various integrals, such as PDEs and ODEs, is the finite element approach [34]; it brings down the ‘mistake’ size[35]. This unique (and essential) step strategy was outlined by Reddy [36] and Jyothi [23]. The literature states that FEM is an effective numerical methodology to discover approximated solutions of PDE and ODE systems that incorporate complex boundary conditions or geometry [24,25]. The FEM is one of the most powerful numerical tools used by developers and users to numerically solve complex types of engineering problems. The sophistication of this technique, its computability, simplicity, accuracy, and efficient results make this method a broadly used technique in boundary value problems. In order to solve Equations (7)–(9) along the boundaries (10), we assume the following:

$$F' = \zeta, \tag{14}$$

System Equations (7)–(10) are transformed to less orders:

$$\left(K + \frac{1}{\chi_1}\right)\zeta'' + \chi_2 F \zeta' - \chi_2 \zeta^2 - M\zeta + \chi_3 \lambda \theta (1 + a \cos \pi \tau) \cos \gamma + KG' - \chi_2 \Omega \frac{\partial \zeta}{\partial \tau}, \tag{15}$$

$$\left(\frac{1}{\chi_1} + \frac{K}{2}\right)G'' + \chi_2 FG' - \chi_2 \zeta G - K(2G + \zeta') - \chi_2 \Omega \frac{\partial G}{\partial \tau}, \tag{16}$$

$$\chi_4 \theta'' + Pr \chi_5 F \theta' - Pr \chi_5 \zeta \theta + Q_s Pr \theta - Pr \chi_5 \Omega \frac{\partial \theta}{\partial \tau}, \tag{17}$$

$$\left. \begin{aligned} F(\tau, \eta = 0) = 0, \zeta(\tau, \eta = 0) = 1, G(\tau, \eta = 0) = 0, \theta(\tau, \eta = 0) = 1, \\ \zeta(\tau, \eta \rightarrow \infty) \rightarrow 0, G(\tau, \eta \rightarrow \infty) \rightarrow 0, \theta(\tau, \eta \rightarrow \infty) \rightarrow 0. \end{aligned} \right\} \tag{18}$$

The fixed numerical estimates of the plate length, border thickness $\tau = 2.0$, and $\eta = 5.0$, respectively. Equations (14)–(17) are provided by

$$\int_{\Omega_e^*} \beta_1 \{F' - \zeta\} d\Omega_e^* = 0, \tag{19}$$

$$\int_{\Omega_e^*} \beta_2 \left\{ \left(\frac{1}{\chi_1} + K\right)\zeta'' + \chi_2 F \zeta' - \chi_2 \zeta^2 - M\zeta + \chi_3 \lambda \theta (1 + a \cos \pi \tau) \cos \gamma + KG' - \chi_2 \Omega \frac{\partial \zeta}{\partial \tau} \right\} d\Omega_e^* = 0, \tag{20}$$

$$\int_{\Omega_e^*} \beta_3 \left\{ \left(\frac{1}{\chi_1} + 0.5K\right)G'' + \chi_2 FG' - \chi_2 \zeta G - K(2G + \zeta') - \chi_2 \Omega \frac{\partial G}{\partial \tau} \right\} d\Omega_e^* = 0, \tag{21}$$

$$\int_{\Omega_e^*} \beta_4 \left\{ \chi_4 \theta'' + Pr \chi_5 F \theta' - Pr \chi_5 \zeta \theta + Q_s Pr \theta - Pr \chi_5 \Omega \frac{\partial \theta}{\partial \tau} \right\} d\Omega_e^* = 0. \tag{22}$$

where $\beta_1, \beta_2, \beta_3$, and β_4 are the arbitrary functions by dividing the domain (Ω_e^*) into four node elements. A finite element’s associated approximations are as follows:

$$F = \sum_{j=1}^4 F_j \Psi_j(\tau, \eta), \zeta = \sum_{j=1}^4 \zeta_j \Psi_j(\tau, \eta), \theta = \sum_{j=1}^4 \theta_j \Psi_j(\tau, \eta). \tag{23}$$

Ψ_j ($j = 1, 2, 3, 4$) are interpolations for rectangular elements Ω_e given by

$$\begin{aligned} \Psi_1 &= \frac{(\tau_{e+1} - \tau)(\eta_{e+1} - \eta)}{(\tau_{e+1} - \tau_e)(\eta_{e+1} - \eta_e)}, & \Psi_2 &= \frac{(\tau - \tau_e)(\eta_{e+1} - \eta)}{(\tau_{e+1} - \tau_e)(\eta_{e+1} - \eta_e)}, \\ \Psi_3 &= \frac{(\tau - \tau_e)(\eta - \eta_e)}{(\tau_{e+1} - \tau_e)(\eta_{e+1} - \eta_e)}, & \Psi_4 &= \frac{(\tau_{e+1} - \tau)(\eta - \eta_e)}{(\tau_{e+1} - \tau_e)(\eta_{e+1} - \eta_e)}. \end{aligned} \tag{24}$$

Finite elements for the equations are given as:

$$\begin{bmatrix} [L^{11}] & [L^{12}] & [L^{13}] & [L^{14}] \\ [L^{21}] & [L^{22}] & [L^{23}] & [L^{24}] \\ [L^{31}] & [L^{32}] & [L^{33}] & [L^{34}] \\ [L^{41}] & [L^{42}] & [L^{43}] & [L^{44}] \end{bmatrix} \begin{bmatrix} \{f\} \\ \{\zeta\} \\ \{g\} \\ \{\theta\} \end{bmatrix} = \begin{bmatrix} \{r_1\} \\ \{r_2\} \\ \{r_3\} \\ \{r_4\} \end{bmatrix} \tag{25}$$

where $[L_{mn}]$ and $[r_m]$ ($m,n=1,2,3,4$) define:

$$\begin{aligned} L_{ij}^{11} &= \int_{\Omega_e^*} \Psi_i \frac{d\Psi_j}{d\eta} d\Omega_e, L_{ij}^{12} = - \int_{\Omega_e} \Psi_i \Psi_j d\Omega_e^*, L_{ij}^{13} = L_{ij}^{14} = L_{ij}^{21} = L_{ij}^{31} = 0 \\ L_{ij}^{22} &= -\left(\frac{1}{\chi_1\chi_2} + K\right) \int_{\Omega_e^*} \frac{d\Psi_i}{d\eta} \frac{d\Psi_j}{d\eta} d\Omega_e^* + \int_{\Omega_e^*} \bar{f}\Psi_i \frac{d\Psi_j}{d\eta} d\Omega_e^* - \int_{\Omega_e^*} \bar{\zeta}\Psi_i \Psi_j d\Omega_e^* - \frac{M}{\chi_2} \int_{\Omega_e^*} \Psi_i \Psi_j d\Omega_e^* - \Omega \int_{\Omega_e^*} \Psi_i \frac{d\Psi_j}{d\tau} d\Omega_e^*, \\ L_{ij}^{23} &= \frac{K}{\chi_2} \int_{\Omega_e^*} \Psi_i \frac{d\Psi_j}{d\eta} d\Omega_e^*, L_{ij}^{24} = \frac{\chi_3\lambda}{\chi_2} (1 + a \cos \pi\tau) \cos \gamma \int_{\Omega_e^*} \Psi_i \Psi_j d\Omega_e^*, \\ L_{ij}^{33} &= -\left(\frac{1}{\chi_1\chi_2} + \frac{K}{2}\right) \int_{\Omega_e^*} \frac{d\Psi_i}{d\eta} \frac{d\Psi_j}{d\eta} d\Omega_e^* + \int_{\Omega_e^*} \bar{f}\Psi_i \frac{d\Psi_j}{d\eta} d\Omega_e^* - \int_{\Omega_e^*} \bar{\zeta}\Psi_i \Psi_j d\Omega_e^* - \frac{2K}{\chi_2} \int_{\Omega_e^*} \Psi_i \Psi_j d\Omega_e^* - \Omega \int_{\Omega_e^*} \Psi_i \frac{d\Psi_j}{d\tau} d\Omega_e^*, \\ L_{ij}^{32} &= -\frac{K}{\chi_2} \Psi_i \frac{d\Psi_j}{d\eta} d\Omega_e^*, L_{ij}^{34} = L_{ij}^{41} = L_{ij}^{42} = L_{ij}^{43} = 0, \\ L_{ij}^{44} &= -\frac{\chi_4}{\chi_5} \int_{\Omega_e^*} \frac{d\Psi_i}{d\eta} \frac{d\Psi_j}{d\eta} d\Omega_e^* + Pr \int_{\Omega_e^*} \bar{f}\Psi_i \frac{d\Psi_j}{d\eta} d\Omega_e^* - Pr \int_{\Omega_e^*} \bar{\zeta}\Psi_i \Psi_j d\Omega_e^* - Pr\Omega \int_{\Omega_e^*} \Psi_i \frac{d\Psi_j}{d\zeta} d\Omega_e^* + Pr \frac{Q_s}{\chi_5} \int_{\Omega_e^*} \bar{\zeta}\Psi_i \Psi_j d\Omega_e^*. \end{aligned}$$

and

$$r_i^1 = 0, r_i^2 = -\left(\frac{1}{\chi_1\chi_2} + K\right) \oint_{\Gamma_e} \Psi_i n_\eta \frac{\partial \bar{q}}{\partial \eta} ds, r_i^3 = -\left(\frac{1}{\chi_1\chi_2} + \frac{K}{2}\right) \oint_{\Gamma_e} \Psi_i n_\eta \frac{\partial \bar{h}}{\partial \eta} ds, r_i^4 = -\frac{\chi_4}{\chi_5} \oint_{\Gamma_e} \Psi_i n_\eta \frac{\partial \bar{\theta}}{\partial \eta} ds. \tag{26}$$

Known values are taken as $\bar{F} = \sum_{j=1}^4 \bar{F}_j \Psi_j$, $\bar{\theta}' = \sum_{j=1}^4 \bar{\theta}'_j \Psi_j$, and $\bar{\zeta} = \sum_{j=1}^4 \bar{\zeta}_j \Psi_j$. The domain is divided into equal grids of rectangular elements 101×101 . We examine each node's four functions. After assembly, we obtained 40,804 non-linear equations; therefore, an iterative method was used to solve them with the necessary 10^{-5} accuracy.

4. Results and Discussion

The results of Equations (7)–(10) are presented in the form of graphs and tables, and then the skin friction coefficient $-F''(\tau, 0)$, thermal transmission $\theta(\tau, \eta)$, micropolar mono, hybrid, and trihybrid nanofluid velocities $F'(\tau, \eta)$, local thermal transmission rate $\theta'(\tau, 0)$, and microrotation $H(\tau, \eta)$. In Figures 2–10, three sets plotted for the above-shown quantities are drawn with respect to three mediums, Al_2O_3 / water, $Al_2O_3-TiO_2$ / water, and $Al_2O_3-TiO_2-SiO_2$ / water. The default quantities of the parameters were $M = K = \lambda = 1.0$, $S_f = 3.0$, $Pr = 0.72$, $\Omega = 0.2$, $a = 0.2$ $\alpha = \pi/4$, $\Phi_1 = 0.06$ (for the monofluid), $\Phi_1 = 0.03$ & $\Phi_2 = 0.3$ (for the hybrid nanofluid), and $\Phi_1 = 0.02$, $\Phi_2 = 0.2$ & $\Phi_3 = 0.2$ (for the trihybrid nanofluid). Compared to the earlier published results, the FEM technique is taken for validity (see Tables 2 and 3).

Table 2. $H'(0)$ & $F''(0)$ against K & M , when $\alpha = a = \lambda = \Omega = 0$.

M	K	Ali et al. [37]		Soaib et al. [38]		Present Results	
		$F''(0)$	$H'(0)$	$F''(0)$	$H'(0)$	$F''(0)$	$H'(0)$
0.0	0.2	−0.90969	0.09499	−0.90979	0.09489	−0.90984	0.09500
0.5	–	−1.11437	0.10509	−1.11438	0.10509	−1.11437	0.10509
1.0	–	−1.28715	0.11206	−1.28715	0.11205	−1.28711	0.11212
1.0	0.0	−1.41421	0.00000	−1.41423	0.00000	−1.41423	0.00000
–	0.5	−1.14078	0.21116	−1.14077	0.21117	−1.14073	0.21116
–	2.0	−0.76975	0.35866	−0.76976	0.35865	−0.76976	0.35861

Table 3. Comparison of $\theta'(0)$ via growing values of Pr when $\lambda = \Omega = \alpha = a = M = 0$.

Pr	Sharidan et al. [7]	Khan et al. [39]	Bagh et al. [40]	Current Results
1.00	−1.0000	−1.0000	−1.00001	−1.000008
3.00	−1.9238	−1.9237	−1.92367	−1.923676
10.0	−3.7225	−3.7207	−3.72067	−3.720669

In Figure 2a,b, $F''(\tau, \eta)$ represents the outcomes that are perceptible in relation to the dimensionless characteristics of dimensionless functions M and K . It appears that the increasing inputs of magnetic parameters M decrease the momentum of fluid. Due to this output, increasing reactions for opposing forces are associated with the development of strength. This can be related to the fact that the growing strength of the magnetic field produces the Lorentz force, which slows down the fluid velocity due to opposing forces [14]. Figure 2b illustrates that the relationship between the material parameter and accelerated bulk flow is direct; $K(K = \kappa/\mu_{nf})$. The viscous effect decreases as the flow inertia increases, leading to a faster flow that may be explained by the growth of K . In Figure 3a,b, the FEM values for the micro-rotation $H(\tau, \eta)$ are plotted where the influences of magnetic and material parameters are observed. Both graphs show that $H(\tau, \eta)$ increases with magnified values of the material parameter K and declines against higher inputs of the magnetic parameter M due to enhancement in the boundary thickness. The temperature distribution graphs $\theta(\tau, \eta)$ in Figure 4a,b reveal that rising values of the magnetic parameter M improve the temperature functions but diminish notably against the rising impact of K . The rising thermal patterns noticed for the growing values of M are common because of the valuable heat-producing from the resistive impact of the Lorentz force [41]. From these figures, the trihybrid nanofluid curves are greater than the curves created by mono and hybrid nanofluids. Hence, ternary nanoparticles are noticed as more efficient at enhancing the base fluid temperature. Trihybrid nanoparticles are more efficient at maximizing thermal performances [42,43].

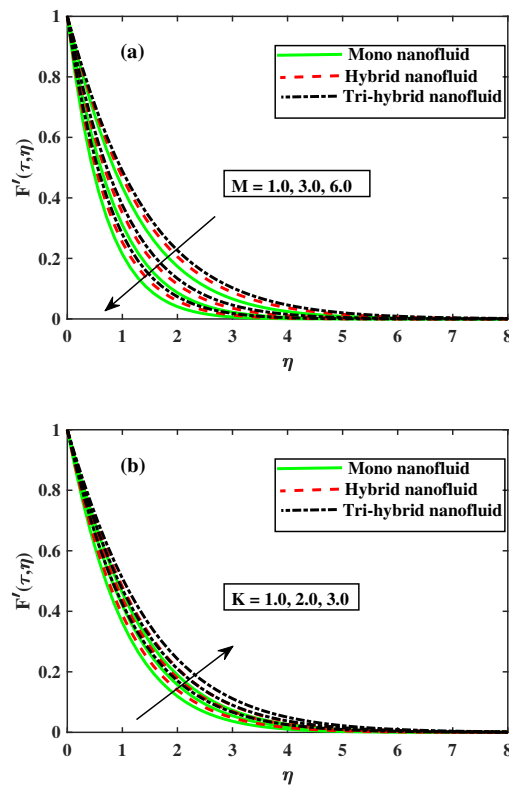


Figure 2. (a) Fluctuation of M on $F'(\tau, \eta)$; (b) Fluctuation of K on $F'(\tau, \eta)$.

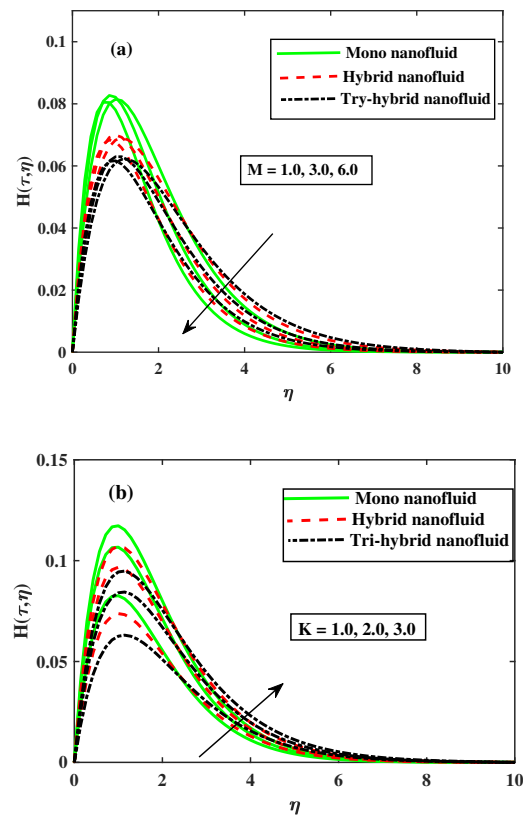


Figure 3. (a) Fluctuation of M on $H(\tau, \eta)$; (b) Fluctuation of K on $H(\tau, \eta)$.

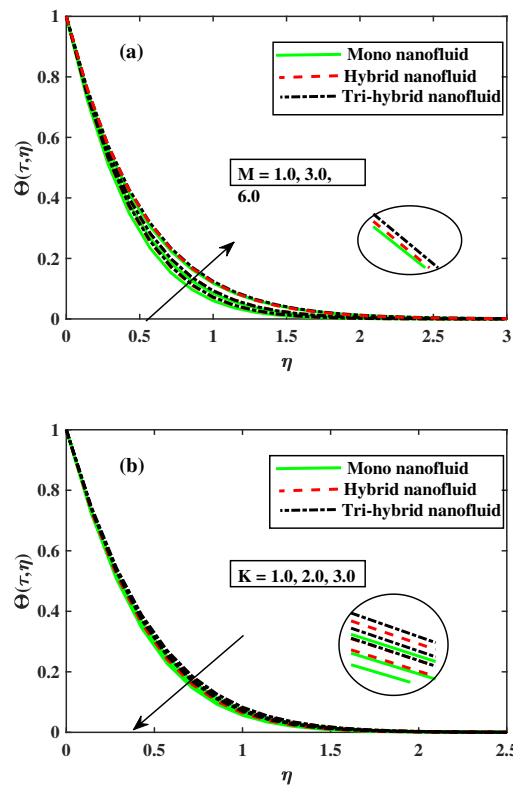


Figure 4. (a) Fluctuation of M on $\theta(\tau, \eta)$; (b) Fluctuation of K on $\theta(\tau, \eta)$.

In Figures 5–8, the skin friction coefficient $Cf_x Re_x^{\frac{1}{2}}$ used variable values of certain parameters that were mapped over normalized time tau . Figure 5a,b, show the fluctuations in velocity gradients with respect to rising values of M and the acceleration modulation a . By increments in the acceleration modulation, skin friction rises; from Figure 5a, it is concluded that $Cf_x Re_x^{\frac{1}{2}}$ also increases by rising magnetic parameters. Skin friction is at its peak in the mono nanofluid case as compared to the trihybrid nanofluid. Figure 6a,b depicts the impacts of the velocity gradient $-F''(\tau, 0)$ according to different values of inclined angles α and acceleration modulation parameters a . It is clear that there is little effect on the velocity gradient by higher inputs of inclination angles and acceleration modulation. By magnified values of both parameters, the velocity gradient increases, but it is at its peak for mono nanofluid compared to the trihybrid nanofluid. Figure 7a,b denotes the impact of the thermal buoyancy parameter and acceleration modulation parameter on the velocity gradient. The velocity gradient at the surface has meager variations as it is influenced by the thermal buoyancy function λ_T and amplitude parameter a , as shown in the figures. Figure 8a,b show how the material parameter K affects skin friction and the local wall thermal transmission. The Nusselt number's & local skin friction coefficient at the surface attained increments by amplified values of material parameters. However, by higher inputs of K , skin friction was at its peak value in the case of mono nanofluid, and the Nusselt number was at its peak value in the case of the trihybrid nanofluid.

Figures 9 and 10 illustrate the surface temperature gradients along τ . From Figure 9a,b, it can be seen that the temperature gradient $-\theta'(\tau, 0)$ fluctuates and increases when the values of the magnetic parameter M and the acceleration parameter a rise. The temperature gradient attains maximum value for trihybrid nanofluid and minimum for mono hybrid nanofluid. Significant characteristics of the gradient of the temperature $-\theta'(\tau, 0)$ exhibited in Figure 9a assured that for the corrected input of the buoyancy parameter λ_T ($\lambda_T = 1.0$) and variation of the acceleration parameter a , there was a significant difference in $-\theta'(\tau, 0)$ for the trihybrid nanofluid and mono nanofluids. Moreover, by contrasting the graphs in Figure 10a,b, it demonstrates that the pattern of fluctuation for $-\theta'(\tau, 0)$ (due to the influence

of modulation parameter a) is more prominent for the fixed value of λ_T ($\lambda_T = 3.0$) than that of $\lambda_T = 1.0$. From both figures, it can be observed that the temperature gradient obtained its peak value for the trihybrid nanofluid.

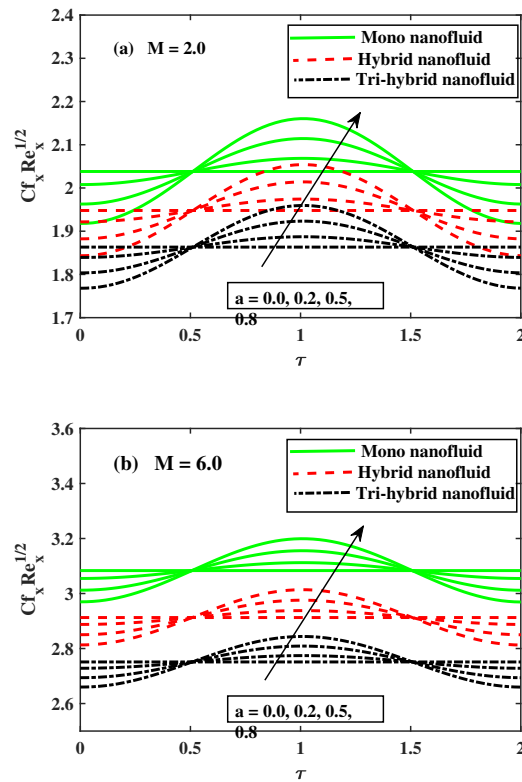


Figure 5. (a) Fluctuation of M on $Cf_x Re_x^{1/2}$; (b) Fluctuation of M on $Cf_x Re_x^{1/2}$.

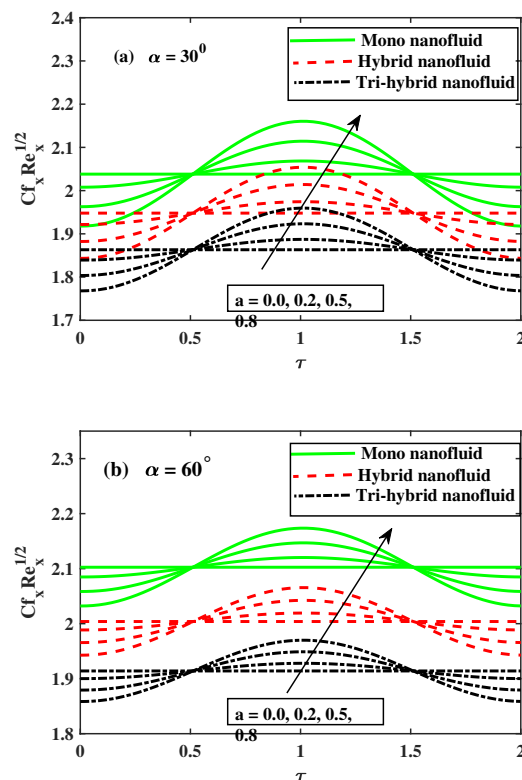


Figure 6. (a) Fluctuation of α on $Cf_x Re_x^{1/2}$; (b) Fluctuation of α on $Cf_x Re_x^{1/2}$.

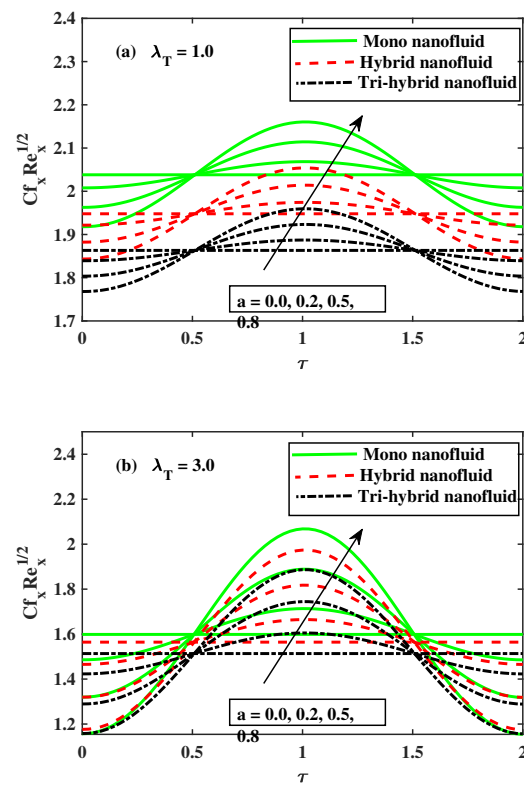


Figure 7. (a) Fluctuation of λ_T on $Cf_x Re_x^{1/2}$; (b) Fluctuation of λ_T on $Cf_x Re_x^{1/2}$.

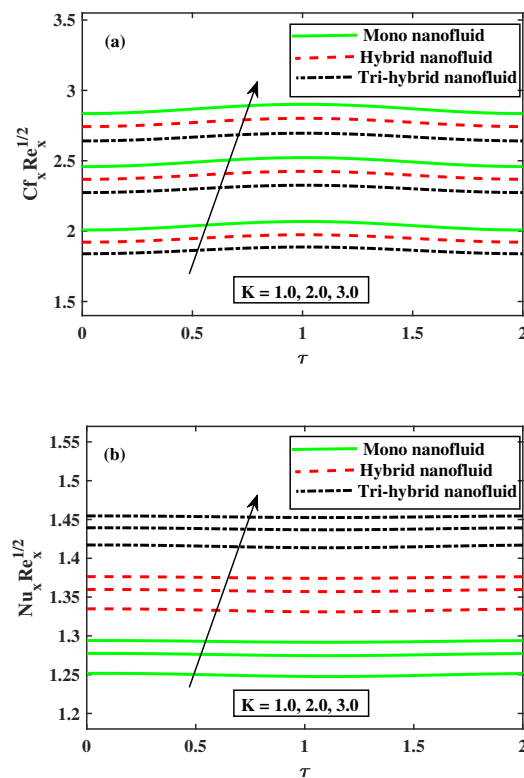


Figure 8. (a) Fluctuation of K on $Cf_x Re_x^{1/2}$; (b) Fluctuation of K on $Nu_x Re_x^{1/2}$.

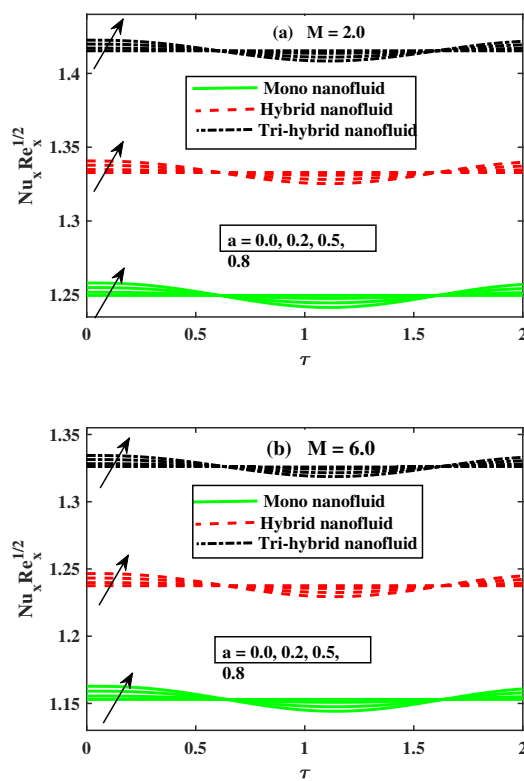


Figure 9. (a) Fluctuation of M on $Nu_x Re_x^{1/2}$; (b) Fluctuation of M on $Nu_x Re_x^{1/2}$.

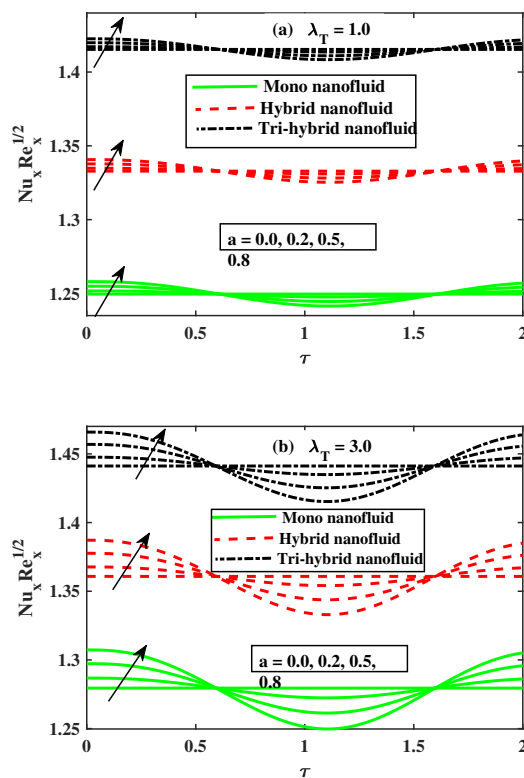


Figure 10. (a) Fluctuation of λ_T on $Nu_x Re_x^{1/2}$; (b) Fluctuation of λ_T on $Nu_x Re_x^{1/2}$.

5. Conclusions

We investigated the importance of the trihybrid nanofluid with G-jitter effects for three colloidal fluid movements, i.e., micropolar nanofluid (copper /water), micropolar hybrid nanofluid (alumina–titanium /water), and micropolar trihybrid nanofluid (alumina–titanium–silicon /water), subjected to the stretch surface. Notable results are given as follows:

- The velocity of fluid $F'(\tau, \eta)$ of mono nanofluids, hybrid nanofluids, and trihybrid nanofluids decelerated in the face of increasing inputs of the magnetic parameter M , and increased against the material parameter K .
- The microrotation $H'(\tau, \eta)$ of mono nanofluids, hybrid nanofluids, and trihybrid nanofluids declined with the growing potential of the magnetic parameter, but when inputs increased, it increased the micropolar material parameter K .
- The temperature of fluid $\theta(\tau, \eta)$ significantly increased the M , but declined against the material parameter $K(K > 0)$.
- Compared to the mono nanofluid flow, the temperature for the tri-nanofluid flow reached greater levels.
- The variation in the decreased skin friction improved with greater inputs of M , $a(a > 0)$ and λ_T . However, it attained a higher peak value for the mono nanofluid compared to the tri-nanofluid.
- Reduced skin friction was better achieved as the plane inclined, but it was worse for mono nanofluids.
- There were increases in the skin friction factor and Nusselt number with material parameter K but the velocity gradient attained a peak value in the case of mono nano fluids; the temperature gradient attained a higher value for the trihybrid nanofluid.
- The larger strength of the magnetic parameter M and acceleration modulation a improved the Nusselt number.
- The Nusselt number varied in the face of λ_T & a and it improved greatly when these parameters increased; the trihybrid nanofluid flow achieved greater values than the nanofluid flow alone.

Author Contributions: Methodology, M.M.A.; Software, S.M.; Validation, N.A.A.; Investigation, A.A.H.; Writing—original draft, B.A.; Writing—review & editing, N.A.S. All authors have read and agreed to the published version of the manuscript.

Funding: The authors extend their appreciation to the Deputyship for Research & Innovation, Ministry of Education, Saudi Arabia, for funding this research work through project number RI-44-0357.

Data Availability Statement: Not applicable.

Acknowledgments: The authors extend their appreciation to the Deputyship for Research & Innovation, Ministry of Education, Saudi Arabia, for funding this research work through project number RI-44-0357.

Conflicts of Interest: The authors declare no conflict of interest.

Nomenclature

\tilde{u}_o	Along x -axis velocity component	\tilde{v}_o	Along x -axis velocity component
\tilde{N}	Angular velocity	\tilde{T}	Temperature of fluid
ρ_{nf}	Nanofluid density	κ	Vortex viscosity
C_p	Specific heat of fluid	μ_{nf}	Dynamical viscosity
$\tilde{\alpha}$	Thermo diffusivity	γ^*	Viscosity spin gradient of fluid
β	Thermal expansion	σ	Electric conduction
K	Material parameter	γ	Inclined angle
B_o	Uniform magnetic field	T_w	Constant surface temperature

T_∞	Ambient value of temperature	M	Magnetic parameter
u_w	Sheet linear velocity	Ω	Dimensionalize frequency
λ	thermal buoyancy	Pr	Prandtl number
Φ_1	First nanoparticle volume fraction	Φ_2	Second nanoparticle volume fraction
Φ_3	Third nanoparticle volume fraction	g	Gravitational acceleration
q_w	Heat flux at surface	Re_x	Reynolds number

References

- Timofeeva, E.V.; Routbort, J.L.; Singh, D. Particle shape effects on thermophysical properties of alumina nanofluids. *J. Appl. Phys.* **2009**, *106*, 014304. [\[CrossRef\]](#)
- Sang, L.; Ai, W.; Wu, Y.; Ma, C. Enhanced specific heat and thermal conductivity of ternary carbonate nanofluids with carbon nanotubes for solar power applications. *Int. J. Energy Res.* **2020**, *44*, 334–343. [\[CrossRef\]](#)
- Mousavi, S.; Esmaeilzadeh, F.; Wang, X. Effects of temperature and particles volume concentration on the thermophysical properties and the rheological behavior of CuO/MgO/TiO₂ aqueous ternary hybrid nanofluid. *J. Therm. Anal. Calorim.* **2019**, *137*, 879–901. [\[CrossRef\]](#)
- Sahoo, R.R.; Kumar, V. Development of a new correlation to determine the viscosity of ternary hybrid nanofluid. *Int. Commun. Heat Mass Transf.* **2020**, *111*, 104451. [\[CrossRef\]](#)
- Abbasi, M.; Heyhat, M.; Rajabpour, A. Study of the effects of particle shape and base fluid type on density of nanofluids using ternary mixture formula: A molecular dynamics simulation. *J. Mol. Liq.* **2020**, *305*, 112831. [\[CrossRef\]](#)
- Sahoo, R.R. Thermo-hydraulic characteristics of radiator with various shape nanoparticle-based ternary hybrid nanofluid. *Powder Technol.* **2020**, *370*, 19–28. [\[CrossRef\]](#)
- Sharidan, S.; Amin, N.; Pop, I. G-jitter mixed convection adjacent to a vertical stretching sheet. *Microgravity-Sci. Technol.* **2006**, *18*, 5. [\[CrossRef\]](#)
- Hamdan, F.R.; Kamal, M.H.A.; Rawi, N.A.; Mohamad, A.Q.; Ali, A.; Ilias, M.R.; Shafie, S. G-jitter Free Convection Flow Near a Three-Dimensional Stagnation-Point Region with Internal Heat Generation. *J. Adv. Res. Fluid Mech. Therm. Sci.* **2020**, *67*, 119–135.
- Tlili, I. Effects MHD and heat generation on mixed convection flow of Jeffrey fluid in microgravity environment over an inclined stretching sheet. *Symmetry* **2019**, *11*, 438. [\[CrossRef\]](#)
- Amin, N. The effect of G-jitter on heat transfer. *Proc. R. Soc. London. A. Math. Phys. Sci.* **1988**, *419*, 151–172.
- Afiqah, R.N.; Rijal, I.M.; Mahat, R.; Mat, I.Z.; Shafie, S. G-jitter induced mixed convection flow of a second grade fluid past an inclined stretching sheet. In *MATEC Web of Conferences*; EDP Sciences: Les Ulis, France, 2018; Volume 189, p. 01006.
- Rawi, N.; Kasim, A.; Isa, M.; Shafie, S. G-jitter Induced MHD Mixed Convection Flow Past an Inclined Stretching Sheet. In *Defect and Diffusion Forum*; Trans Tech Publications Ltd.: Bäch, Switzerland, 2015; Volume 362, pp. 76–83.
- Shehzad, N.; Zeeshan, A.; Shakeel, M.; Ellahi, R.; Sait, S.M. Effects of magnetohydrodynamics flow on multilayer coatings of Newtonian and non-Newtonian fluids through porous inclined rotating channel. *Coatings* **2022**, *12*, 430. [\[CrossRef\]](#)
- Awan, A.U.; Majeed, S.; Ali, B.; Ali, L. Significance of nanoparticles aggregation and Coriolis force on the dynamics of Prandtl nanofluid: The case of rotating flow. *Chin. J. Phys.* **2022**, *79*, 264–274. [\[CrossRef\]](#)
- Ali, B.; Shafiq, A.; Manan, A.; Wakif, A.; Hussain, S. Bioconvection: Significance of mixed convection and mhd on dynamics of Casson nanofluid in the stagnation point of rotating sphere via finite element simulation. *Math. Comput. Simul.* **2022**, *194*, 254–268. [\[CrossRef\]](#)
- Koriko, O.; Omowaye, A.; Animasaun, I.L.; Bamisaye, M.E. Melting heat transfer and induced-magnetic field effects on the micropolar fluid flow towards stagnation point: Boundary layer analysis. *Int. J. Eng. Res. Afr.* **2017**, *29*, 10–20. [\[CrossRef\]](#)
- Abiev, R.S. Mathematical model of two-phase Taylor flow hydrodynamics for four combinations of non-Newtonian and Newtonian fluids in microchannels. *Chem. Eng. Sci.* **2022**, *247*, 116930. [\[CrossRef\]](#)
- Chabani, I.; Mebarek-Oudina, F.; Ismail, A.A.I. MHD Flow of a Hybrid Nanofluid in a Triangular Enclosure with Zigzags and an Elliptic Obstacle. *Micromachines* **2022**, *13*, 224. [\[CrossRef\]](#)
- Bhatti, M.; Arain, M.; Zeeshan, A.; Ellahi, R.; Doranehgard, M. Swimming of Gyrotactic Microorganism in MHD Williamson nanofluid flow between rotating circular plates embedded in porous medium: Application of thermal energy storage. *J. Energy Storage* **2022**, *45*, 103511. [\[CrossRef\]](#)
- Al-Farhany, K.; Abdulkadhim, A.; Hamzah, H.K.; Ali, F.H.; Chamkha, A. MHD effects on natural convection in a U-shaped enclosure filled with nanofluid-saturated porous media with two baffles. *Prog. Nucl. Energy* **2022**, *145*, 104136. [\[CrossRef\]](#)
- Jang, J.; Lee, S.S. Theoretical and experimental study of MHD (magnetohydrodynamic) micropump. *Sens. Actuators A Phys.* **2000**, *80*, 84–89. [\[CrossRef\]](#)
- Mahariq, I.; Giden, I.H.; Alboon, S.; Aly, W.H.F.; Youssef, A.; Kurt, H. Investigation and analysis of acoustojets by spectral element method. *Mathematics* **2022**, *10*, 3145. [\[CrossRef\]](#)
- Jyothi, K.; Reddy, P.S.; Reddy, M.S. Carreau nanofluid heat and mass transfer flow through wedge with slip conditions and nonlinear thermal radiation. *J. Braz. Soc. Mech. Sci. Eng.* **2019**, *41*, 415. [\[CrossRef\]](#)
- Ali, B.; Yu, X.; Sadiq, M.T.; Rehman, A.U.; Ali, L. A Finite Element Simulation of the Active and Passive Controls of the MHD Effect on an Axisymmetric Nanofluid Flow with Thermo-Diffusion over a Radially Stretched Sheet. *Processes* **2020**, *8*, 207. [\[CrossRef\]](#)

25. Ali, B.; Hussain, S.; Naqvi, S.I.R.; Habib, D.; Abdal, S. Aligned Magnetic and Bioconvection Effects on Tangent Hyperbolic Nanofluid Flow Across Faster/Slower Stretching Wedge with Activation Energy: Finite Element Simulation. *Int. J. Appl. Comput. Math.* **2021**, *7*, 149. [[CrossRef](#)]
26. Rawi, N.A.; Zin, N.A.M.; Kasim, A.R.M.; Shafie, S. G-jitter induced MHD mixed convection flow of nanofluids past a vertical stretching sheet. In *AIP Conference Proceedings*; AIP Publishing LLC: Melville, NY, USA, 2016; Volume 1750, p. 030017.
27. Kumar, L. Finite element analysis of combined heat and mass transfer in hydromagnetic micropolar flow along a stretching sheet. *Comput. Mater. Sci.* **2009**, *46*, 841–848. [[CrossRef](#)]
28. Ali, B.; Hussain, S.; Nie, Y.; Ali, L.; Hassan, S.U. Finite Element Simulation of Bioconvection and Cattaneo-Christov Effects On Micropolar Based Nanofluid Flow Over a Vertically Stretching Sheet. *Chin. J. Phys.* **2020**, *66*, 682–689. [[CrossRef](#)]
29. Ali, B.; Naqvi, R.A.; Ali, L.; Abdal, S.; Hussain, S. A Comparative Description on Time-Dependent Rotating Magnetic Transport of a Water Base Liquid H_2O With Hybrid Nano-materials Al_2O_3-Cu and $Al_2O_3-TiO_2$ Over an Extending Sheet Using Buongiorno Model: Finite Element Approach. *Chin. J. Phys.* **2021**, *70*, 125–139. [[CrossRef](#)]
30. Devi, S.S.U.; Devi, S.A. Numerical investigation of three-dimensional hybrid $Cu-Al_2O_3$ /water nanofluid flow over a stretching sheet with effecting Lorentz force subject to Newtonian heating. *Can. J. Phys.* **2016**, *94*, 490–496. [[CrossRef](#)]
31. Khatib, R.; Schwalm, J.D.; Yusuf, S.; Haynes, R.B.; McKee, M.; Khan, M.; Nieuwlaat, R. Patient and healthcare provider barriers to hypertension awareness, treatment and follow up: A systematic review and meta-analysis of qualitative and quantitative studies. *PLoS ONE* **2014**, *9*, e84238. [[CrossRef](#)]
32. Hamid, M.; Usman, M.; Zubair, T.; Haq, R.U.; Wang, W. Shape effects of MoS_2 nanoparticles on rotating flow of nanofluid along a stretching surface with variable thermal conductivity: A Galerkin approach. *Int. J. Heat Mass Transf.* **2018**, *124*, 706–714. [[CrossRef](#)]
33. Rostami, M.N.; Dinarvand, S.; Pop, I. Dual solutions for mixed convective stagnation-point flow of an aqueous silica–alumina hybrid nanofluid. *Chin. J. Phys.* **2018**, *56*, 2465–2478. [[CrossRef](#)]
34. Ali, B.; Pattnaik, P.; Naqvi, R.A.; Waqas, H.; Hussain, S. Brownian motion and thermophoresis effects on bioconvection of rotating Maxwell nanofluid over a Riga plate with Arrhenius activation energy and Cattaneo-Christov heat flux theory. *Therm. Sci. Eng. Prog.* **2021**, *23*, 100863. [[CrossRef](#)]
35. Reddy, G.J.; Raju, R.S.; Rao, J.A. Influence of viscous dissipation on unsteady MHD natural convective flow of Casson fluid over an oscillating vertical plate via FEM. *Ain Shams Eng. J.* **2018**, *9*, 1907–1915. [[CrossRef](#)]
36. Reddy, J.N. *Solutions Manual for an Introduction to the Finite Element Method*; McGraw-Hill: New York, NY, USA, 1993; p. 41.
37. Ali, L.; Liu, X.; Ali, B.; Mujeed, S.; Abdal, S. Finite Element Simulation of Multi-Slip Effects on Unsteady MHD Bioconvective Micropolar nanofluid Flow Over a Sheet with Solutal and Thermal Convective Boundary Conditions. *Coatings* **2019**, *9*, 842. [[CrossRef](#)]
38. Abdal, S.; Ali, B.; Younas, S.; Ali, L.; Mariam, A. Thermo-Diffusion and Multislip Effects on MHD Mixed Convection Unsteady Flow of Micropolar Nanofluid over a Shrinking/Stretching Sheet with Radiation in the Presence of Heat Source. *Symmetry* **2020**, *12*, 49. [[CrossRef](#)]
39. Khan, S.A.; Nie, Y.; Ali, B. Multiple slip effects on MHD unsteady viscoelastic nanofluid flow over a permeable stretching sheet with radiation using the finite element method. *SN Appl. Sci.* **2020**, *2*, 66. [[CrossRef](#)]
40. Ali, L.; Liu, X.; Ali, B.; Mujeed, S.; Abdal, S. Finite Element Analysis of Thermo-Diffusion and Multi-Slip Effects on MHD Unsteady Flow of Casson NanoFluid over a Shrinking/Stretching Sheet with Radiation and Heat Source. *Appl. Sci.* **2019**, *9*, 5217. [[CrossRef](#)]
41. Vanita; Kumar, A. Numerical study of effect of induced magnetic field on transient natural convection over a vertical cone. *Alex. Eng. J.* **2016**, *55*, 1211–1223. [[CrossRef](#)]
42. Oke, A.S. Heat and Mass Transfer in 3D MHD Flow of EG-Based Ternary Hybrid Nanofluid Over a Rotating Surface. *Arab. J. Sci. Eng.* **2022**, *47*, 16015–16031. [[CrossRef](#)]
43. Sajid, T.; Ayub, A.; Shah, S.Z.H.; Jamshed, W.; Eid, M.R.; El Din, E.S.M.T.; Irfan, R.; Hussain, S.M. Trace of chemical reactions accompanied with arrhenius energy on ternary hybridity nanofluid past a wedge. *Symmetry* **2022**, *14*, 1850. [[CrossRef](#)]

Disclaimer/Publisher’s Note: The statements, opinions and data contained in all publications are solely those of the individual author(s) and contributor(s) and not of MDPI and/or the editor(s). MDPI and/or the editor(s) disclaim responsibility for any injury to people or property resulting from any ideas, methods, instructions or products referred to in the content.